Nanoscale

PAPER

View Article Online
View Journal | View Issue

Cite this: *Nanoscale*, 2015, **7**, 5446

High reduction of interfacial charge recombination in colloidal quantum dot solar cells by metal oxide surface passivation†

Jin Chang,*[a,b] Yuki Kuga,[a] Iván Mora-Seró,[c] Taro Toyoda,[a,b] Yuhei Ogomi,[d,b] Shuzi Hayase,[d,b] Juan Bisquert[c,e] and Qing Shen*[a,b]

Bulk heterojunction (BHJ) solar cells based on colloidal QDs and metal oxide nanowires (NWs) possess unique and outstanding advantages in enhancing light harvesting and charge collection in comparison to planar architectures. However, the high surface area of the NW structure often brings about a large amount of recombination (especially interfacial recombination) and limits the open-circuit voltage in BHJ solar cells. This problem is solved here by passivating the surface of the metal oxide component in PbS colloidal quantum dot solar cells (CQDSCs). By coating thin TiO_2 layers onto ZnO-NW surfaces, the open-circuit voltage and power conversion efficiency have been improved by over 40% in PbS CQDSCs. Characterization by transient photovoltage decay and impedance spectroscopy indicated that the interfacial recombination was significantly reduced by the surface passivation strategy. An efficiency as high as 6.13% was achieved through the passivation approach and optimization for the length of the ZnO-NW arrays (device active area: 16 mm^2). All solar cells were tested in air, and exhibited excellent air storage stability (without any performance decline over more than 130 days). This work highlights the significance of metal oxide passivation in achieving high performance BHJ solar cells. The charge recombination mechanism uncovered in this work could shed light on the further improvement of PbS CQDSCs and/or other types of solar cells.

Received 20th December 2014,
Accepted 4th February 2015

DOI: 10.1039/c4nr07521h

www.rsc.org/nanoscale

Introduction

Colloidal quantum dots (CQDs) have attracted significant attention in the last two decades due to their unique optoelectronic properties in various applications such as light emitting diodes, field effect transistors,[1] photovoltaic cells,[2,3] photo-detectors,[4] and bio-imaging.[5] Their particular advantages in low-temperature fabrication, solution-based processing, bandgap tunability *via* the quantum size effect, and possibility of multi-exciton generation (MEG) have presented them as promising light-absorbing materials in various photovoltaic applications.[6–10]

Colloidal quantum dot solar cells (CQDSCs) – presently dominated by lead chalcogenide-based solar cells – have emerged as a new class of solar cells with efficiencies showing continuous progress and, recently, promising results in long term stability.[11,12] Metal oxide/quantum dot heterojunction solar cells have been recently introduced and have shown several advantages over previous architectures such as Schottky quantum dot solar cells.[13] This structure was initially demonstrated by Aydil and coworkers in solar cells consisting of n-type ZnO and p-type PbSe QDs.[3,14] ZnO/PbS CQDSCs were subsequently reported by Nozik and co-workers in 2010, resulting in the first certified efficiency of 3% for this type of device.[8] The following years have seen a significant increase in the photovoltaic performances of CQDSCs with the development in CQD surface passivation strategies.[2,15–18] Recently, a certified efficiency of 8.6% has been reported by Bawendi and co-workers for planar ZnO/PbS CQDSCs, which further indicates the great potential of CQDSCs.[11] Although the highest efficiency was obtained using the planar structure, it does not mean that this structure is the most favourable configuration. In CQDSCs, the photocurrent density, J_{sc}, is limited by the low

[a]*Faculty of Informatics and Engineering, The University of Electro-Communications, 1-5-1 Chofugaoka, Chofu, Tokyo 182-8585, Japan. E-mail: jin@jupiter.pc.uec.ac.jp, shen@pc.uec.ac.jp; Fax: +8142 443 5501; Tel: +81 42 443 5471*
[b]*CREST, Japan Science and Technology Agency (JST), 4-1-8 Honcho, Kawaguchi, Saitama 332-0012, Japan*
[c]*Photovoltaic and Optoelectronic Devices Group, Department de Física, Universitat Jaume I, 12071 Castelló, Spain*
[d]*Faculty of Life Science and Systems Engineering, Kyushu Institute of Technology, 2-4 Hibikino, Wakamatsu-ku, Kitakyushu, Fukuoka 808-0196, Japan*
[e]*Department of Chemistry, Faculty of Science, King Abdulaziz University, Jeddah, Saudi Arabia*
†Electronic supplementary information (ESI) available. See DOI: 10.1039/c4nr07521h

carrier diffusion length (<100 nm),[19,20] which means that only the photogenerated charge at the depleted region plus the diffusion length could be collected. This fact limits the thickness of the CQD layer (~300 nm), to be insufficient to absorb all incident above-bandgap solar radiation.[20] Nanostructured TiO_2 pillars[21] and ZnO nanowire (NW) arrays[22,23] have been explored in order to enhance the light-harvesting capacity using thicker CQD layers interpenetrated by the NW arrays. This strategy is efficient in boosting the photocurrent density to values higher than 30 mA cm^{-2}.[23] But, on the other hand, this strategy also increases the recombination loss due to the increase in the interfacial area between NWs and CQDs, thus decreasing the device performance, especially the open circuit voltage (V_{oc}).[22,23]

Previous investigations into CQDSCs have been mainly focused on the properties of CQD suspensions and films. Studies on the metal oxide component have been rarely reported and have been mostly focused on their morphological properties and the effect of doping.[24–26] The surface passivation of the metal oxide or interface engineering at the metal oxide/quantum dot interfaces has attracted less attention, but could be similarly important. In addition, reducing the charge recombination is one of the most important ways to achieve high efficiency photovoltaic devices. Considerable emphasis has been placed on the interface recombination at the metal oxide/light absorber interfaces in various photovoltaic technologies, such as dye-sensitized solar cells (DSSCs), quantum-dot-sensitized solar cells (QDSSCs), and organic photovoltaics (OPVs).[25,27–31] For example, TiO_2 layers were introduced by Cao and co-workers to modify the surface of mesoporous ZnO electrodes, which improved the photovoltaic performances of CdS/CdSe QDSSCs.[32] Similarly, MgO layers were also employed to modify the electrode surfaces and prevent the recombination loss in CdS QDSSCs.[33] Although the charge recombination mechanism in heterojunction CQDSCs is thought to be different from that in liquid-based QDSSCs,[25] introducing a thin passivation layer is expected to reduce the surface states of the metal oxide (such as ZnO-NWs) and enhance their photovoltaic properties in CQDSCs.

Here we report the preparation of PbS CQDSCs using ZnO-NWs as the selective contact for electrons, improving the V_{oc} and power convention efficiency (PCE) by over 40% through the metal oxide surface passivation strategy. A maximum efficiency of over 6% has been achieved through the further optimization of the length of the ZnO-NW arrays. The photo-generated charge recombination mechanism in CQDSCs was revealed through open-circuit transient voltage decay measurements. It was revealed that the metal oxide passivation strategy significantly reduced the interfacial recombination in PbS CQDSCs. In addition, the prepared devices possess a remarkable long term stability of more than 130 days in air. Our results highlight the significance of metal oxide surface passivation in heterojunction CQDSCs and the elucidation of the recombination mechanism in these devices, which would shed light on the further improvement of cell performances.

Experimental

Materials

Zinc acetate dehydrate ($Zn(OAc)_2{\cdot}2H_2O$, 99.9%), ethanolamine (99.0%), 2-methoxyethanol (99.0%), zinc nitrate hexahydrate ($Zn(NO_3)_2{\cdot}6H_2O$, 99.0%), hexamethylenetetramine (HMTA, 99.0%), boric acid (H_3BO_3, 99.5%), lead oxide (PbO, 99.5%), oleic acid (OA, technical grade, 60%), cadmium chloride ($CdCl_2$, 95.0%), hexadecyltrimethylammonium bromide (CTAB, 99.0%), and oleylamine (OLA, 99.0%) were purchased from Wako Pure Chemical Industries. Ammonium hexafluorotitanate ($(NH_4)_2TiF_6$, 99.99%), 1-octadecene (ODE, 95.0%), tetradecylphosphonic acid (TDPA, 97%), and hexamethyldisilathiane (TMS, synthesis grade) were purchased from Sigma-Aldrich. All chemicals were used as received without purification.

Preparation of ZnO-NWs

ZnO-NW arrays were grown on FTO glasses pre-coated with compact seed layers by a modified literature method.[22] Fig. 1 illustrates the basic procedure for the synthesis of the NW arrays. To prepare the sol–gel precursor for the ZnO compact layer, zinc acetate dehydrate and ethanolamine were dissolved in 2-methoxyethanol to obtain the 0.5 M zinc precursor (Zn^{2+} solution-1). Then, 300 μL of Zn^{2+} solution-1 was dropped onto cleaned FTO glasses (25 mm × 25 mm) and spun-cast at 1000 rpm for 2 s plus 3500 rpm for 60 s, followed by baking at temperature T1 for 10 min in air. These spin-coat and annealing processes were repeated to generate a uniform ZnO compact seed layer with a thickness of around 100 nm. To grow ZnO-NWs, the seed-coated FTO substrates were floated face down in Scott bottles containing the aqueous Zn^{2+} solution-2 (25 mM zinc nitrate hexahydrate and 25 mM HMTA), and heated at 90 °C for 2–4 h. After growth, the substrates

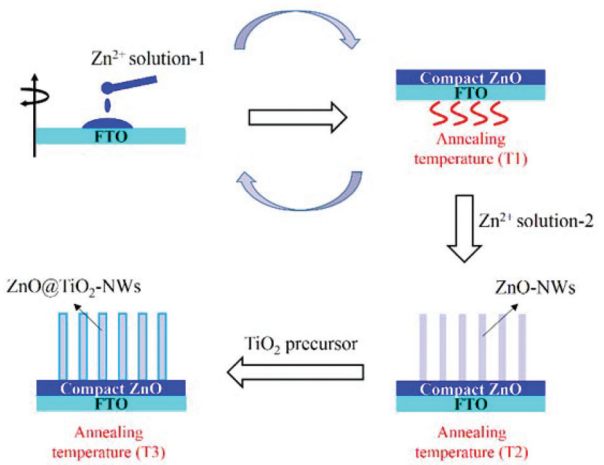

Fig. 1 Schematic illustration of the fabrication of ZnO-NWs and the surface passivation by coating with TiO_2. Zn^{2+} solution-1 contains zinc acetate and ethanolamine in 2-methoxyethanol. Zn^{2+} solution-2 is an aqueous solution containing zinc nitrate hexahydrate and hexamethylenetetramine. The TiO_2 precursor is an aqueous solution containing ammonium hexafluorotitanate and boric acid.

were rinsed with pure water, dried with a nitrogen flow, and annealed at temperature T2 for 30 min.

Preparation of ZnO@TiO_2-NWs

It is well known that ZnO nanocrystals usually possess significant numbers of surface defects, as reflected by their unique defective emission in the visible light range.[34] In photovoltaic applications, the undesired defects often act as recombination sites and reduce the device performance. To reduce the surface defects of the ZnO-NWs, thin TiO_2 layers were coated onto the ZnO surfaces because TiO_2 possesses a similar band structure but a smaller number of defects compared with the ZnO counterpart.[35] The TiO_2 layers were grown by a chemical bath deposition (CBD) method. Typically, the ZnO-NW arrays were immersed in a TiO_2 precursor containing an equal molar ratio of $(NH_4)_2TiF_6$ and H_3BO_3 for 5 s at 10 °C. The concentration of the TiO_2 precursor solution was adjusted over the range of 1–25 mM to optimize the thickness of the TiO_2 layer. After coating with TiO_2, the substrates were rinsed with pure water, dried with a nitrogen flow, and annealed at temperature T3 for 30 min.

Synthesis of PbS QDs

Colloidal PbS QDs were synthesized according to a modified literature method.[2] In this work, 6 mmol PbO and 15 mmol OA were mixed with 50 mL ODE in a 100 mL three-neck flask. The mixture was stirred and degassed at room temperature and then at 100 °C for 30 min and 1 h, respectively. The solution was then heated to 120 °C under nitrogen for another 1 h, followed by the injection of TMS solution (3 mmol TMS mixed with 10 mL pre-degassed ODE) at 115 °C. After injection, the heater was removed immediately while stirring of the solution was maintained. When the solution was cooled to 75 °C, a $CdCl_2$–TDPA–OLA solution containing 1 mmol $CdCl_2$, 0.1 mmol TDPA, and 3 mL OLA was injected into the colloidal PbS. After cooling down to room temperature, the reaction solution was mixed with 150 mL acetone and centrifuged at 4000 rpm for 5 min to precipitate PbS QDs. The obtained precipitate was re-dispersed in 20 mL toluene, washed with 40 mL acetone followed by centrifugation. This purification process was repeated twice to remove the unbound OA ligands from the colloidal PbS. After purification, the obtained PbS QD precipitate was dried by a nitrogen flow and dispersed in 15 mL octane. The concentration of colloidal PbS was approximately 50 mg mL^{-1} assuming that the reactant TMS was completely transformed into the PbS product.

Fabrication of PbS CQDSCs

To fabricate PbS heterojunction solar cells, PbS colloidal QDs were deposited on ZnO-NW and ZnO@TiO_2-NW arrays by a typical layer-by-layer method using a fully automatic spin-coater. Each spin-coating cycle consisted of three steps: PbS deposition, ligand exchange, and solvent rinse. Generally, colloidal PbS (100 μL) was dropped onto NW array-coated FTO substrates and spun-cast at 2500 rpm for 15 s. Then, CTAB solution (30 mM in methanol) was dropped onto the substrate and spun dry after a 60 s wait. The ligand exchange step was conducted twice to ensure complete ligand exchange with the oleic acid that was capping the PbS surfaces. The substrate was then rinsed three times with methanol to remove excess unbound ligands. For typical ZnO/PbS solar cells, this spin-cast process was repeated for 20–25 cycles depending on the length of the NW arrays. Finally, a 100 nm Au contact was thermally evaporated onto the PbS layer through a mask to create four identical cells on each substrate. Control solar cells with the planar architecture were fabricated by spin-coating PbS layers onto compact ZnO layers with identical methods as described above. The thickness of the ZnO and PbS layers was 100 nm and 300 nm, respectively.

Device characterization

The current density–voltage (J–V) measurements were performed using a Keithley 2400 source meter in the dark and under AM 1.5 G irradiation (100 mW cm^{-2}), with a Peccell solar simulator PEC-L10. The IPCE spectra were recorded under illumination using a Nikon G250 monochromator equipped with a 300 W Xe arc lamp. The transient open-circuit voltage decay measurements were carried out using a 532 nm diode laser with a pulse duration of 5 ns and repetition rate of 4 Hz. The voltage responses were recorded using an Iwatsu digital oscilloscope DS-5554. The transient voltage decay measurements were taken without a background light bias. The electrochemical impedance spectroscopy (EIS) measurements were performed in the dark using an impedance analyser (BioLogic, SP-300) by applying a small voltage perturbation (10 mV rms) at frequencies from 1 MHz to 0.1 Hz for different forward bias voltages.

Other characterization

The morphology of the ZnO-NWs and ZnO@TiO_2-NWs was examined using a scanning electron microscope (SEM, JEOL, JSM-6340) and a transmission electron microscope (TEM, JEOL, JEM-2010). The elemental composition of the ZnO@TiO_2-NWs was determined using a scanning electron microscope equipped with an energy dispersive X-ray (EDX) spectroscope. The UV-vis-NIR absorption spectra of the NW arrays and PbS QDs were recorded using a spectrophotometer (JASCO, V-670). The florescence spectra of the NW arrays were recorded using a spectrofluorometer (JASCO, FP-6500). The average size of the PbS QDs was determined by a transmission electron microscope (TEM, JEOL, JEM-2010). The photoelectron yield spectra of the ZnO and PbS films were recorded using an ionization energy measurement system (Model BIP-KV205, Bunkoukeiki Co, Ltd).

Results and discussion

Growth and surface passivation of ZnO-NWs

To obtain a homogeneous metal oxide/PbS bulk heterojunction with a high electron collection efficiency, a uniform metal oxide nanostructure with minimal surface defects is required.

In this work, ZnO-NW and ZnO@TiO_2-NW (TiO_2 passivated ZnO-NW) arrays were prepared by wet-chemical methods as illustrated in Fig. 1. The annealing temperatures (T1, T2 and T3 as shown in Fig. 1) for each preparation step and the TiO_2 precursor concentration were optimized to achieve uniform NW arrays with minimal surface defects. After coating zinc solution-1 onto the FTO substrates, the obtained ZnO compact layers were annealed at 150 °C in air (see optimization details in ESI†), followed by the growth of the ZnO-NWs in zinc solution-2. The side view SEM image of the optimized ZnO-NWs is shown in Fig. 2a, with a length of approximately 1.6 μm. Fig. 2b displays the corresponding TEM and high resolution transmission electron microscopy (HR-TEM) images, showing that the NWs are 34 nm in diameter and possess interplanar distances of 0.26 nm along the *c*-axis of the ZnO-NWs.

For the surface passivation of the ZnO-NWs, thin TiO_2 layers were grown onto the ZnO surfaces by immersing the arrays into an aqueous TiO_2 precursor containing $(NH_4)_2TiF_6$ and H_3BO_3. The TiO_2 layers were obtained through the etching of ZnO and the chemical reaction between ZnO and the TiO_2 precursor according to the following equation:[36]

$$ZnO + 2TiF_6^{2-} + 2H_3BO_3 \rightarrow Zn^{2+} + 2TiO_2 + 4F^- + 2BF_4^- + 3H_2O$$

As shown in the above equation, one portion of ZnO can be dissolved in the TiF_6^{2-}/H_3BO_3 solutions to form two portions of TiO_2 *in situ*. Therefore, the average diameter of the ZnO-NWs should be slightly increased after treatment with TiO_2, depending on the dissolution degree of the ZnO-NWs. Meanwhile, the roughness of the ZnO surfaces should also be increased due to the etching of the TiO_2 precursor onto ZnO. To minimize the effect of TiO_2 treatment on the ZnO morphologies, the TiO_2 precursor with low concentrations (1.0, 2.5 and 5.0 mM) was employed to treat the ZnO-NWs. High concentration precursors were employed as control experiments, which exhibited poor device performances. Fig. 2c presents the top view SEM image of the ZnO-NW arrays treated with the 5.0 mM TiO_2 precursor, which shows a similar diameter to bare ZnO-NWs. The energy dispersive X-ray spectroscopy (EDX) image shown in Fig. S2† confirmed the formation of TiO_2 after annealing. The TEM image of the ZnO@TiO_2-NWs is shown in Fig. 2d. It is evident that the ZnO surfaces were coated with a rough TiO_2 layer with a thickness in the range of 3–5 nm.

To evaluate the effects of annealing temperatures and surface passivation on ZnO surface defects, room-temperature photoluminescence (PL) studies were carried out for the obtained samples. Firstly, the as-prepared bare ZnO-NWs were annealed at temperature T2 (300–450 °C, see Fig. 1) to investigate the effect of the annealing temperature on the PL spectra of the ZnO-NWs. As displayed in Fig. S3,† all of the ZnO-NW samples exhibited a narrow UV emission at approximately 378 nm, which can be attributed to the near band edge transitions in ZnO. A broad visible emission centered at around 600 nm could be attributed to the oxygen vacancies on the ZnO surfaces.[37] The PL spectrum of the as-prepared ZnO-NWs was similar to that of the samples annealed at 300 °C and 350 °C, except for a slight red-shift in the visible emission for the annealed samples. As the annealing temperature was increased to 400–450 °C, the surface defect-originated emission was greatly increased with a consequent decrease in the UV emission. Therefore, the optimal annealing temperature was determined to be 350 °C for lowest defect emission and sufficient ZnO crystallinity. The annealed ZnO-NWs were then treated with the TiO_2 precursors, followed by annealing at temperature T3 (see Fig. 1) for 30 min. Similarly, the annealing temperature T3 was also optimized to 350 °C, as shown in Fig. S4.† The effect of TiO_2 treatment on the PL spectra of the ZnO-NWs is shown in Fig. 3. After passivation with TiO_2, the intensity of the visible emission was dramatically decreased,

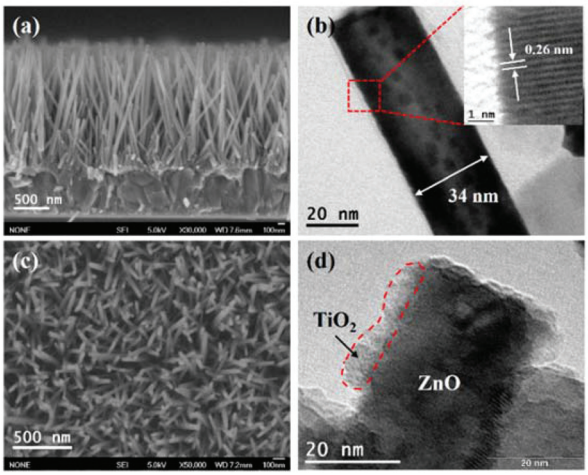

Fig. 2 (a) Side view SEM image of the ZnO-NW arrays with a length of approximately 1.6 μm; (b) TEM image of bare ZnO-NW with a diameter of 34 nm; the inset HR-TEM image shows the interplanar distance of 0.26 nm along the *c*-axis; (c) top view SEM image of the ZnO@TiO_2-NW arrays; (d) TEM image of ZnO@TiO_2-NW, showing ZnO surfaces coated with a TiO_2 layer with a thickness of 3–5 nm.

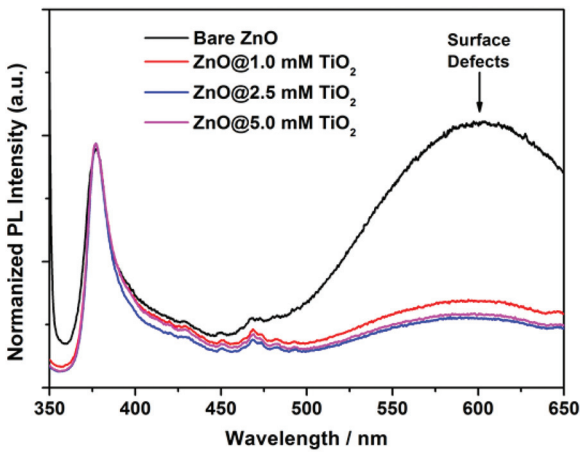

Fig. 3 Room temperature PL spectra of bare ZnO-NW arrays and the arrays treated with the TiO_2 precursors of different concentrations (1.0, 2.5 and 5.0 mM) at 10 °C for 5 s.

suggesting that the defects on the ZnO surfaces were largely eliminated by the TiO_2 layer. Note that a slight variation in passivation is observed by changing the precursor concentration. The reduction in the surface defects of the ZnO-NWs could be mainly due to the fact that TiO_2 usually possesses a smaller number of surface states compared to ZnO.[35]

Characterization and photovoltaic performance of PbS CQDSCs

PbS CQDSCs based on the ZnO-NWs and ZnO@TiO_2-NWs were fabricated by the layer-by-layer spin coating method with ligand exchange.[2] Oleic acid (OA)-capped colloidal PbS QDs were spun cast onto FTO substrates with NW arrays. A cetyltrimethylammonium bromide (CTAB) solution was applied for the solid state ligand exchange of the PbS films, followed by a rinse step to remove unbound excess ligands. The TEM image shows that the average size of the PbS QDs employed in this work is approximately 3.5 nm (Fig. S5a†). The first exciton absorption peak of OA-capped PbS was 1040 nm for both the colloidal suspension and the thin films. A red shift was observed after ligand exchange with CTAB (Fig. S5b†), indicating the enhanced interaction between closely packed PbS QDs.[38] The spin coat cycles were repeated until the NW arrays were filled with PbS QDs, obtaining an overlayer of approximately 200 nm on top of the arrays. Au electrodes with a thickness of approximately 100 nm were deposited onto the PbS layer by a thermal evaporation method. Fig. 4a and b illustrate the structure of the ZnO@TiO_2/PbS solar cells employed in this work, with four parallel cells on each FTO substrate. Fig. 4c and d display the photographs of the PbS CQDSCs before and after the deposition of the Au contacts, showing the mirror-like PbS film fabricated in our laboratory. The cross-section SEM image of the fabricated cells is presented in Fig. 4e, which confirmed the bulk heterojunction structure of the fabricated cells. It also shows that the PbS QDs have successfully infiltrated and are evenly distributed between the NW arrays. We observed that the fabrication of void-free PbS films was necessary to achieve high-efficiency solar cells. A high spin-coat speed (at least 2500 rpm) for colloidal PbS and sufficient time being spun-dry (15 s) were critical to obtain void-free PbS films. The active area under illumination was defined as 16 mm^2 (4 mm × 4 mm) by a photomask. Note that the active area is significantly larger than typical values (~1–5 mm^2) reported in previous literature.[11,15,22,23]

Fig. 5a shows the diagram of energy level alignment in FTO/ZnO@TiO_2/PbS/Au solar cells. The energy levels of ZnO and PbS were estimated from the photoelectron yield spec-

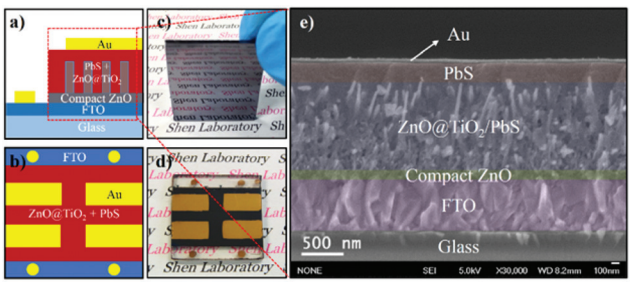

Fig. 4 (a, b) A schematic illustration of the ZnO@TiO_2/PbS solar cells; (c, d) photographs of the PbS CQDSCs before and after the deposition of the Au contacts; (e) a typical cross-section SEM image of the ZnO@TiO_2/PbS solar cells.

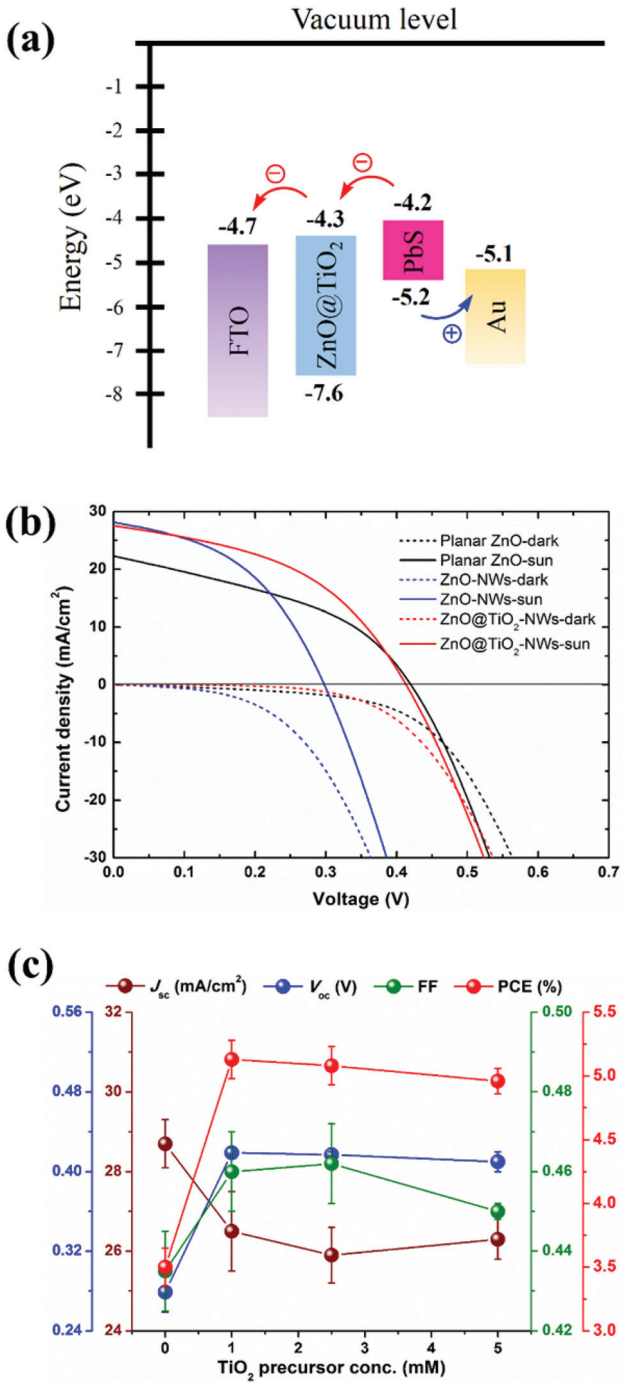

Fig. 5 (a) Schematic energy level diagram of FTO/ZnO@TiO_2/PbS/Au solar cells. (b) Comparison of the photocurrent density–voltage (J–V) curves of PbS CQDSCs based on planar ZnO and ZnO-NWs with or without TiO_2 treatment. (c) Effects of the TiO_2 precursor concentration on the J_{sc}, V_{oc}, FF, and PCE values of the ZnO-NWs/PbS CQDSCs.

troscopy (PYS) and UV-vis-NIR measurements (Fig. S5–S7†), while the work function values of FTO and Au were taken from published literature.[23] Control planar samples (PCE = 3.8%, J_{sc} = 22.3 mA cm^{-2}, V_{oc} = 0.42 V, and fill factor (FF) = 0.41) were prepared. Compared to the planar PbS CQDSC, the bare ZnO-NW device exhibited higher J_{sc} values, but relatively lower V_{oc}, in accordance with our expectation, while both present similar FF (Fig. 5b). Notably, through the surface passivation approach, the V_{oc} of the ZnO-NW based solar cell was significantly improved from approximately 0.3 V up to 0.42 V without an obvious decline in J_{sc} (Fig. 5b). This means that the decreased V_{oc} value caused by the increased interface area of the NWs was well-recovered by the surface passivation approach. Consequently, devices prepared with properly-passivated ZnO-NWs present significantly higher photocurrent and similar V_{oc} for a higher final performance in comparison with the planar architecture. The plots in Fig. 5c show the detailed effects of TiO_2 treatment on the J_{sc}, V_{oc}, fill factor (FF), and PCE of ZnO-NWs-based PbS CQDSCs. It was shown that V_{oc} was greatly improved from approximately 0.3 V for a bare ZnO cell up to 0.42 V for ZnO@TiO_2 cells; approximately a 40% enhancement. The PCE was enhanced essentially by the same amount, from 3.5% to 5%, as the decrease observed in the photocurrent is compensated for by an increase in FF.

Note that both the planar and NW architectures present low FF; this fact cannot be attributed to the cell configuration but instead to the QD preparation. Further organic, inorganic or hybrid passivation of the colloidal QDs will help to enhance this parameter.[15] Passivation of the QDs will also enhance the V_{oc}. However, the use of nanowires results in photocurrent enhancement and subsequent use of passivation removes the deleterious effect introduced by the enhanced recombination.

The slight decrease in J_{sc} after treatment with TiO_2 could be attributed to the fact that the TiO_2 layers probably affected the injection of electrons from the PbS QDs to the ZnO-NWs because TiO_2 possesses lower electron mobility than ZnO-NWs.[34,39] This was supported by our observation that J_{sc} decreased dramatically when higher concentrations of the TiO_2 precursors and/or longer treatment times were employed (see Fig. S8 and Table S1†). It is noted that the J_{sc} value was nearly the same for TiO_2 precursor concentrations in the range of 1.0–5.0 mM, except for the lower value in the case of 2.5 mM. This could be due to the structural complexity of bulk heterojunction CQDSCs. A slight deviation in photovoltaic performance might occur if any voids exist within the PbS films, although identical fabrication procedures were strictly controlled in our work. Nevertheless, it can be seen that the J_{sc} value for the ZnO-NW arrays was reduced after treatment with TiO_2, and the effect was more obvious in the case of higher TiO_2 precursor concentrations. The incident photon-to-current efficiency (IPCE) spectra of the fabricated cells are shown in Fig. S9,† with calculated photocurrents consistent with the measured J_{sc} values. ZnO@TiO_2/PbS devices exhibited lower IPCE values than that of the bare ZnO/PbS device at longer wavelengths, which was consistent with the J–V results. Since the light is incident from the FTO, long-wavelength photons are able to penetrate deeper into the solar cells due to the smaller absorption coefficient of the PbS QDs at longer wavelengths (Fig. S5b†). Electrons generated by long-wavelength photons have to travel a long distance to arrive at the FTO substrate along the NW arrays. The decrease of IPCE in the ZnO@TiO_2/PbS devices at longer wavelengths indicated a lower photocurrent collection efficiency in comparison with that of the bare ZnO/PbS device.

The difference in photovoltaic properties between bare ZnO/PbS and the surface-passivated ZnO@TiO_2/PbS cells could also be observed from the dark current curves as shown in Fig. 5b. The obtained PbS quantum dot solar cells show a clear decrease in overall dark current upon surface passivation of ZnO. This decrease could be attributed to the reduction of recombination at the ZnO@TiO_2/PbS interface, because the dark current in p–n junction solar cells is mainly dominated by the recombination close to the junction.[25] A high defect density at the ZnO/PbS interface would allow carriers to move to these recombination sites very quickly and recombine, thus increasing the dark current.

To explore the mechanism of the photovoltaic enhancement in surface passivated ZnO/PbS solar cells, transient open-circuit photovoltage decay measurements were carried out. Through investigating the open-circuit photovoltage decay behaviour, the charge recombination mechanism in solar cells could be extracted. Upon illumination, photo-generated electrons were injected from the PbS QDs to the ZnO-NWs while holes remained in the PbS QD films, forming the photovoltage V_{oc} within the ZnO/PbS junctions under open-circuit conditions. When the incident light is switched off, photo-generated charges could recombine through various paths, leading to the decay in V_{oc} until returning to the thermal equilibrium state (see the illustration in Fig. 6c). Fig. 6a shows the transient photovoltage decay curves of our PbS CQDSCs. It was evident that the ZnO@TiO_2/PbS cells exhibited much slower decay processes than those of the bare ZnO/PbS cell, which provided direct proof of the reduced recombination in the surface-passivated cells. In addition, the decay curves could be roughly divided into two sections: (i) a very fast decay process that occurred in the initial stage and (ii) a slow decay process with a sample-dependent timescale. To quantitatively analyse the voltage decay processes, the voltage decay curves were fitted with a dual exponential decay plus an offset according to the following equation:

$$y(t) = A_1 e^{-t/\tau_1} + A_2 e^{-t/\tau_2} + A_3 \quad (1)$$

where A_1, A_2 and A_3 are proportionality constants, and τ_1 and τ_2 are time constants. The fitted curves and the corresponding parameters are shown in Fig. S10† and Table 1, respectively. For eqn (1), we assigned the first exponential decay to the fast voltage decay process (section 1), while the second exponential decay and the offset correspond to the slow voltage decay process (section 2). According to fitted data, the time constant τ_1 was similar for passivated and non-passivated cells considering the ultrafast timescale and fitting uncertainty. Notably,

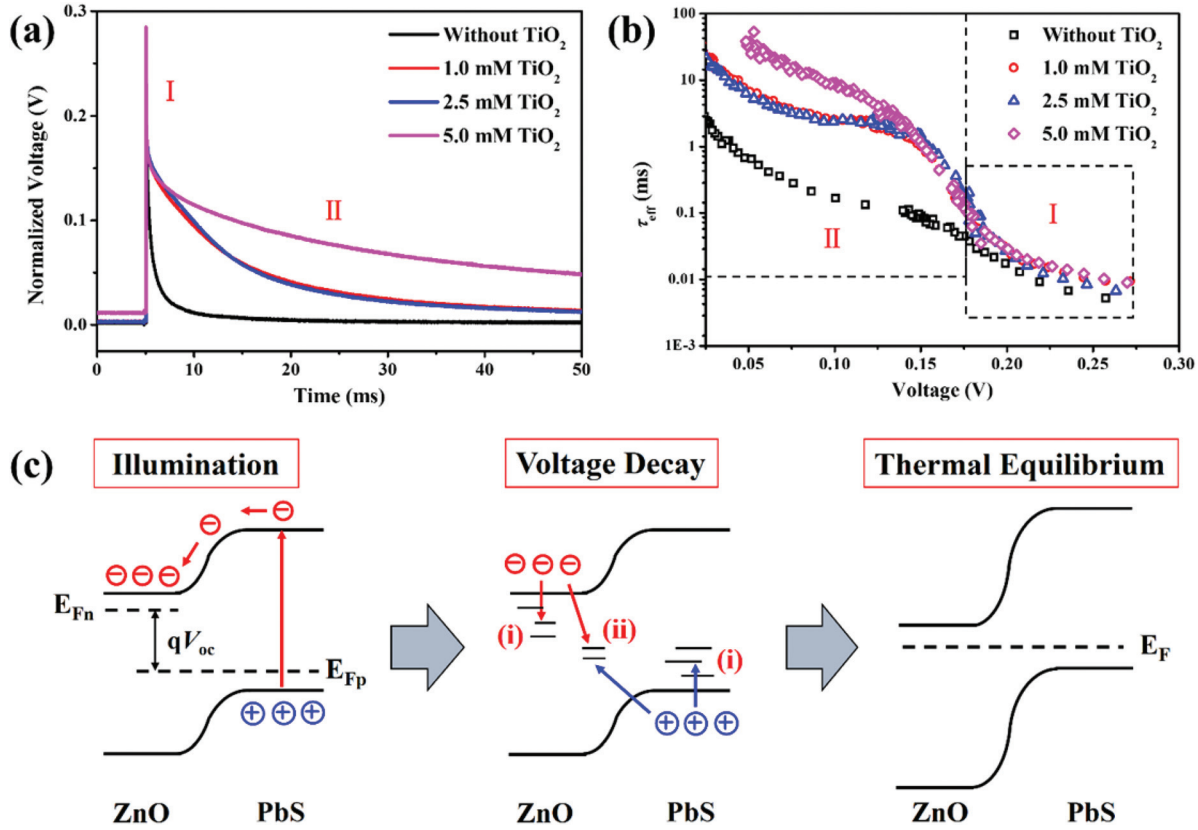

Fig. 6 (a) Normalized open-circuit photovoltage decay curves for ZnO/PbS CQDSCs with and without the TiO_2 coating on the ZnO-NWs, showing two dominant decay processes. (b) The effective carrier lifetime calculated from the voltage decay curves. (c) Schematic illustration of the energy level alignment in the PbS CQDSCs during the voltage decay measurement. The voltage decay process is mainly attributed to two recombination paths: (i) intrinsic trapping-assisted recombination in ZnO and the PbS films and (ii) interfacial recombination at the ZnO/PbS interfaces.

Table 1 Fitted proportionality constants (including the relative weight) and time constants obtained from the open-circuit photovoltage decay curves of the PbS CQDSCs

Cells	A_1 ($A_1/(A_1+A_2+A_3)$)	τ_1 (ms)	A_2 ($A_2/(A_1+A_2+A_3)$)	τ_2 (ms)	A_3 ($A_3/(A_1+A_2+A_3)$)
Without TiO_2	0.15 (76%)	0.044 ± 0.002	0.044 (22%)	3.23 ± 0.03	0.0032 (1%)
1.0 mM TiO_2	0.11 (41%)	0.062 ± 0.0005	0.14 (52%)	8.81 ± 0.01	0.015 (7%)
2.5 mM TiO_2	0.11 (40%)	0.037 ± 0.0005	0.15 (55%)	8.37 ± 0.006	0.014 (5%)
5.0 mM TiO_2	0.09 (39%)	0.18 ± 0.02	0.098 (42%)	17.6 ± 0.05	0.043 (19%)

the weight of A_1 decreased from 76% to 39% after the surface passivation of ZnO. This could be due to the reduction in surface defects in passivated ZnO (as supported by the PL results in Fig. 3), *i.e.*, the reduction in electron trapping on ZnO surfaces. The remaining A_1 weight (approximately 40%) probably corresponds to hole trapping in the PbS QDs and trapping of remaining electrons in ZnO. For the slow voltage decay process, the time constant τ_2 increased from 3.23 ms to 17.6 ms after passivation of ZnO. The prolonged charge recombination process in the passivated cells was mainly attributed to the reduced interfacial recombination at the ZnO/PbS interfaces.

In addition to the voltage decay analysis, we also evaluated the recombination processes based on the effective carrier lifetime (τ_{eff}), which can be defined by the follow equations (see details in the ESI†):[40,41]

$$\tau_{eff} = -\left(\frac{kT}{q}\right)\Big/\left(\frac{dV_{oc}}{dt}\right) = 1/(\tau_n^{-1} + \tau_p^{-1}) \quad (2)$$

$$\tau_n^{-1} = \frac{(dn/dt)}{n} \quad (3)$$

$$\tau_p^{-1} = \frac{(dp/dt)}{p} \quad (4)$$

where k is the Boltzmann constant, T is the temperature, q is the elementary charge, n is the free electron density in the ZnO-NWs and p is the free hole density in the PbS QDs. τ_n and τ_p are the

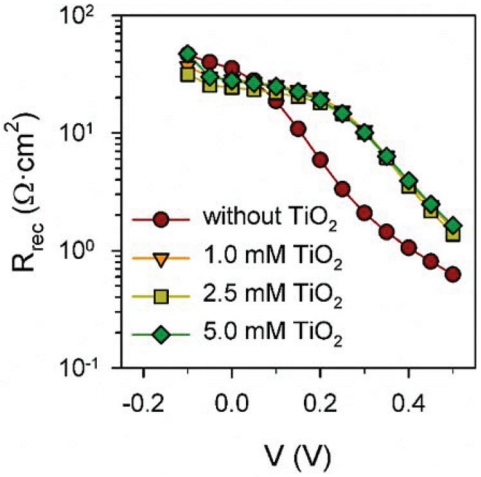

Fig. 7 Recombination resistance obtained from impedance spectroscopy analysis.

free electron lifetime in the ZnO-NWs and the free hole lifetime in the PbS QDs, respectively. According to the above equations, the open-circuit photovoltage decay is dependent on both the electron and hole lifetimes in p–n junction CQDSCs.

As shown in Fig. 6b, the photovoltage-dependent effective carrier lifetime could also be divided into two sections, corresponding to the two photovoltage decay processes. In the high V_{oc} regime (section I in Fig. 6b), the value of τ_{eff} was below 0.1 ms and nearly the same for both passivated and non-passivated devices. We propose that this regime could be assigned to a bulk recombination mechanism. In the low V_{oc} regime (section II in Fig. 6b), the values of τ_{eff} in the passivated cells were 1–2 orders of magnitude higher than that of the non-passivated cell. This confirmed again that the second voltage decay process was dominated by interfacial recombination at the ZnO/PbS interfaces. Based on the above experimental results, it was concluded that the surface passivation of metal oxide films significantly reduced interfacial recombination, thus enhancing the V_{oc} and PCE in the ZnO/PbS CQDSCs. According to our voltage decay analysis, bulk recombination has to be reduced using other strategies such as QD passivation.[15]

In addition to the transient photovoltage decay measurements, impedance spectroscopy measurements were also conducted to verify the reduction in interfacial recombination in passivated ZnO/PbS CQDSCs. The impedance technique has been extensively employed in the characterization of a variety of photovoltaic devices,[42–44] but it has not been employed significantly in the characterization of CQDSCs. This technique allows easy measurement of the recombination resistance, R_{rec}, which is inversely proportional to the recombination rate. Fig. 7 shows a clear enhancement of R_{rec} after coating TiO_2

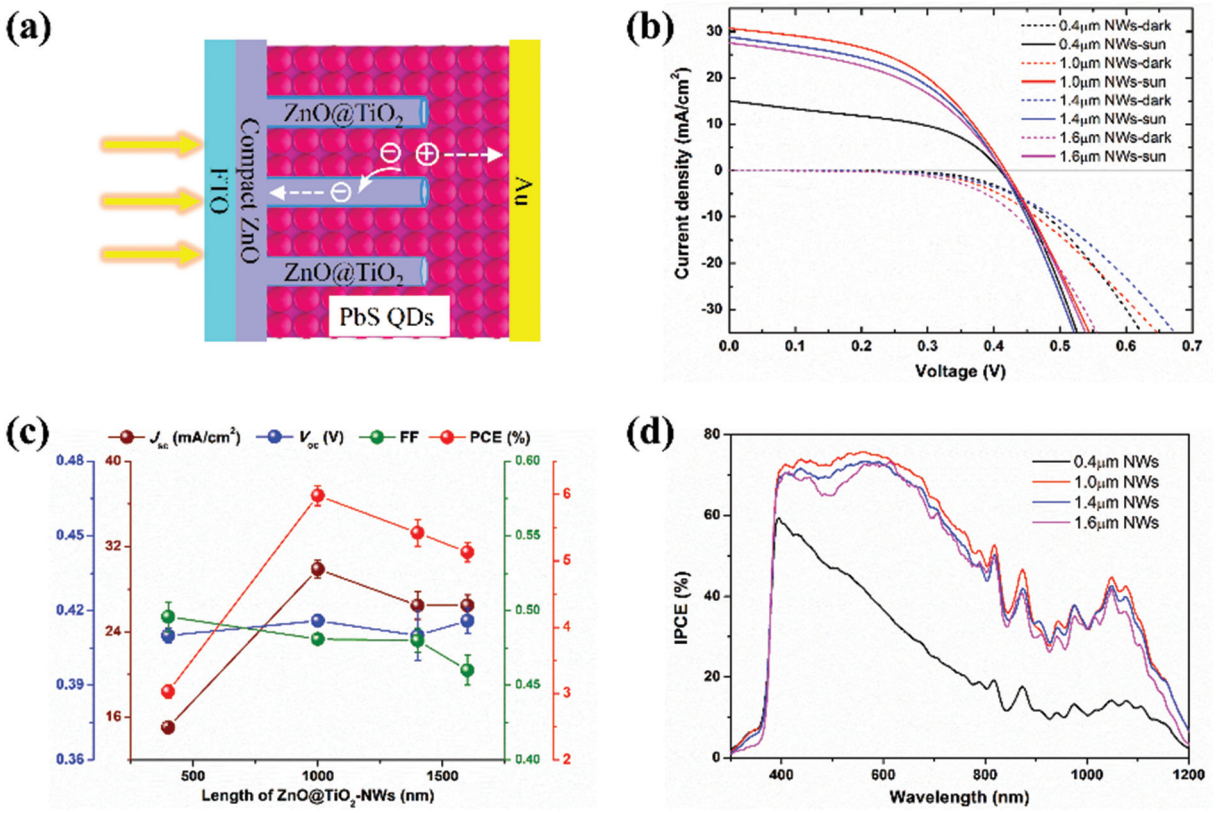

Fig. 8 (a) Schematic illustration of the photogenerated carrier collection in the ZnO@TiO_2/PbS cells. (b) J–V curves of the PbS CQDSCs based on ZnO@TiO_2-NWs with different NW lengths. (c) Effects of the NW length on the J_{sc}, V_{oc}, FF and PCE of the PbS CQDSCs. (d) IPCE spectra of the ZnO@TiO_2/PbS cells with different lengths of NW arrays, with the calculated photocurrent consistent with the measured J_{sc} values.

onto the ZnO-NW surfaces, indicating a reduction in the recombination rate and causing the increase in V_{oc} observed for these devices. This result was consistent with the voltage decay analysis as discussed above.

Effect of the NW length and device stability

In addition to that of surface passivation, the effect of the NW length on the photovoltaic performance of the ZnO@TiO_2/PbS cells was also investigated. It is known that bulk heterojunction PbS cells possess the advantages of high light absorption and effective carrier extraction owing to the short carrier diffusion length of their nanostructures. As the device thickness increases, the harvesting of light can be enhanced; however, the photo-generated current density often decreases when the thickness is beyond the limitation of effective carrier collection. Considering these effects, it is important to optimize the length of the NW arrays in our ZnO@TiO_2/PbS devices.

Fig. S12† shows the cross-section SEM images of ZnO-NW arrays grown on FTO substrates, with growth times varying from 2 to 4 hours. Short ZnO-NWs with lengths of about 400 nm were obtained when the growth time was 2 h. When the growth time was prolonged to 3, 3.5, and 4 h, corresponding ZnO-NWs with lengths of 1000 nm, 1400 nm, and 1600 nm were obtained. ZnO-NWs of different lengths were then immersed in 1.0 mM TiF_6^{2-}/H_3BO_3 solutions for 5 s to form the ZnO@TiO_2-NWs. After treatment withTiO_2, the PbS CQDSCs were fabricated by the same procedure as described before (see details in the Experimental section). Fig. 8a illustrates the photogenerated carrier collection in the ZnO@TiO_2/PbS solar cells. Fig. 8b shows the *J*–*V* curves of PbS CQDSCs with different lengths of ZnO@TiO_2-NW arrays. The detailed effects of NW length on the J_{sc}, V_{oc}, FF, and PCE are displayed in Fig. 8c. When the NW length was increased from 0.4 μm to 1 μm, J_{sc} increased from approximately 15 to over 30 mA cm^{-2}. This could be due to the increase in the loading of PbS QDs in longer NW arrays, leading to the enhancement in light harvesting. Then, J_{sc} decreased slightly as the NW length was further increased to 1.6 μm. This could be attributed to a decrease in charge collection efficiency as the length of the NW array increased. Similarly, the FF values decreased as the NW length increased, which could be mainly attributed to the increase in resistances and surface defects in NWs. By contrast, the V_{oc} values were independent of the NW length. The highest PCE of 6.13% was obtained for the cell with NW length of 1 μm, which was the best result for the PbS CQDSCs based on ZnO-NWs. The corresponding IPCE spectra are shown in Fig. 8d, with the calculated photocurrent consistent with the measured J_{sc} values.

In addition to the cell efficiencies, their stability and reproducibility are also important factors for the overall evaluation of solar cells. Hysteresis has been identified as a big problem for the correct determination of cell efficiency in various types of photovoltaic devices. Therefore, we have carefully evaluated the hysteresis in our PbS CQDSCs, as shown in Fig. 9b and S13.† No significant hysteric effect (lower than 1%) has been identified for our CQDSC devices. Furthermore, we have evaluated the long term stability of the prepared devices. As can be seen in Fig. 9a, both the ZnO/PbS and the ZnO@TiO_2/PbS devices exhibited excellent long-term storage stability for over 130 days (>3000 h). All solar cells were stored and tested in an ambient atmosphere. During the course of the stability assessment, the cells were stored in air under dark conditions without the control of humidity. All of the photovoltaic parameters exhibited overall increase as the storage time continued. The most interesting part is that the J_{sc} and the FF in the ZnO/PbS and ZnO@TiO_2/PbS devices approached the same values after storage for over 60 days. By contrast, the difference in V_{oc} narrowed during the initial 40 days, then remained at around 0.09 V. The improvement in V_{oc}, therefore, enhanced the PCE value for the ZnO@TiO_2/PbS cells and maintained it, or even enhanced it in the long term.

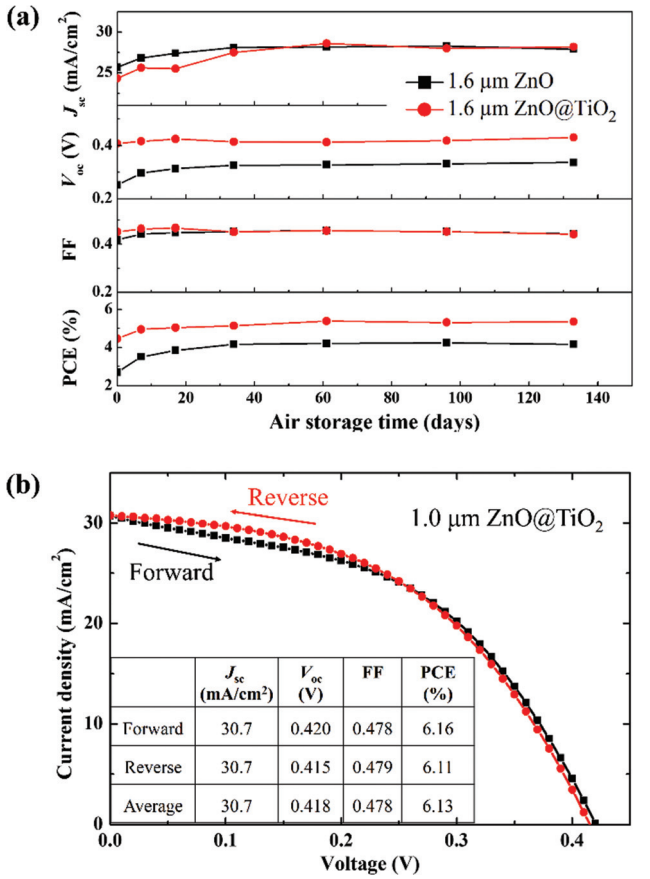

Fig. 9 (a) Stability evaluation of the bare and surface-passivated PbS CQDSCs with NW arrays of 1.6 μm length. All devices were stored and tested in an ambient atmosphere. (b) *J*–*V* curves of a NW length-optimized ZnO@TiO_2/PbS cell measured by forward (short circuit → open circuit) and reverse (open circuit → short circuit) scans with 10 mV voltage steps and 200 ms delay times under AM 1.5 G illumination.

Conclusion

In summary, we have confirmed the beneficial role of ZnO NWs in order to enhance CQDSC photocurrent. In addition,

we have significantly improved the photovoltaic performances of PbS BHJ CQDSCs by introducing passivation layers onto electron-selective substrates (ZnO-NWs), which was proved to reduce the interfacial recombination at the ZnO/PbS interfaces. The surface defects of the ZnO-NWs were significantly reduced by coating 3–5 nm thick TiO_2 layers onto the ZnO surfaces and annealing the NW arrays at an optimized temperature (350 °C). Our results show that a low TiO_2 precursor concentration (1–5 mM) was effective in passivating the ZnO-NWs and improving the photovoltaic properties, while a high precursor concentration (>12.5 mM) was detrimental to our devices. A dramatic improvement (over 40%) in V_{oc} and PCE was finally achieved through the optimized surface passivation strategy for the ZnO-NWs arrays.

The mechanism behind this achievement was explored using open-circuit voltage decay and impedance spectroscopy techniques. It was revealed that the metal oxide passivation strategy significantly reduced the interfacial recombination in the PbS CQDSCs. This conclusion was supported by the impedance spectroscopy characterization, which shows increased recombination resistance in passivated solar cells. By analysing the voltage decay curves, we observed that bulk recombination in the QD layer is another bottleneck in the performance of CQDSCs, which accounts for approximately 40% of the total charge recombination. Colloidal QD passivation should reduce this recombination as it has been previously reported. Consequently, even higher efficiencies can be expected in the future for CQDSCs with NW architectures. Through the metal oxide passivation strategy and the optimization of the length of ZnO-NWs, a maximum efficiency of 6.13% has been achieved, which is currently the highest efficiency for PbS CQDSCs based on ZnO-NWs. This result is quite outstanding in consideration of the active area (16 mm^2), which is much larger than those used in previous literature. The device stability and measurement method were also evaluated, which shows negligible hysteric effect in our devices and excellent storage stability in air (without any performance decline over 130 days). In short, this study highlights the significance of metal oxide passivation in achieving high efficiency bulk heterojunction solar cells. The charge recombination mechanism characterized in this work could shed light on the further improvement of PbS CQDSCs and/or other types of solar cells.

Acknowledgements

This research was supported by the Japan Science and Technology Agency (JST) CREST program and MEXT KAKENHI grant number 26286013.

Notes and references

1 J.-S. Lee, M. V. Kovalenko, J. Huang, D. S. Chung and D. V. Talapin, *Nat. Nanotechnol.*, 2011, **6**, 348–352.
2 J. Tang, K. W. Kemp, S. Hoogland, K. S. Jeong, H. Liu, L. Levina, M. Furukawa, X. Wang, R. Debnath, D. Cha, K. W. Chou, A. Fischer, A. Amassian, J. B. Asbury and E. H. Sargent, *Nat. Mater.*, 2011, **10**, 765–771.
3 K. S. Leschkies, T. J. Beatty, M. S. Kang, D. J. Norris and E. S. Aydil, *ACS Nano*, 2009, **3**, 3638–3648.
4 G. Konstantatos, I. Howard, A. Fischer, S. Hoogland, J. Clifford, E. Klem, L. Levina and E. H. Sargent, *Nature*, 2006, **442**, 180–183.
5 K. Zagorovsky and W. C. W. Chan, *Nat. Mater.*, 2013, **12**, 285–287.
6 H. Lee, H. C. Leventis, S.-J. Moon, P. Chen, S. Ito, S. A. Haque, T. Torres, F. Nüesch, T. Geiger, S. M. Zakeeruddin, M. Grätzel and M. K. Nazeeruddin, *Adv. Funct. Mater.*, 2009, **19**, 2735–2742.
7 G. I. Koleilat, L. Levina, H. Shukla, S. H. Myrskog, S. Hinds, A. G. Pattantyus-Abraham and E. H. Sargent, *ACS Nano*, 2008, **2**, 833–840.
8 J. M. Luther, J. Gao, M. T. Lloyd, O. E. Semonin, M. C. Beard and A. J. Nozik, *Adv. Mater.*, 2010, **22**, 3704–3707.
9 A. Luque, A. Martí and A. J. Nozik, *MRS Bull.*, 2007, **32**, 236–241.
10 O. E. Semonin, J. M. Luther, S. Choi, H.-Y. Chen, J. Gao, A. J. Nozik and M. C. Beard, *Science*, 2011, **334**, 1530–1533.
11 C.-H. M. Chuang, P. R. Brown, V. Bulović and M. G. Bawendi, *Nat. Mater.*, 2014, **13**, 796–801.
12 H. Wang, T. Kubo, J. Nakazaki and H. Segawa, *Phys. Status Solidi RRL*, 2014, **8**, 961–965.
13 K. W. Johnston, A. G. Pattantyus-Abraham, J. P. Clifford, S. H. Myrskog, D. D. MacNeil, L. Levina and E. H. Sargent, *Appl. Phys. Lett.*, 2008, **92**, 151115.
14 K. S. Leschkies, A. G. Jacobs, D. J. Norris and E. S. Aydil, *Appl. Phys. Lett.*, 2009, **95**, 193103.
15 A. H. Ip, S. M. Thon, S. Hoogland, O. Voznyy, D. Zhitomirsky, R. Debnath, L. Levina, L. R. Rollny, G. H. Carey, A. Fischer, K. W. Kemp, I. J. Kramer, Z. Ning, A. J. Labelle, K. W. Chou, A. Amassian and E. H. Sargent, *Nat. Nanotechnol.*, 2012, **7**, 577–582.
16 Z. Ning, Y. Ren, S. Hoogland, O. Voznyy, L. Levina, P. Stadler, X. Lan, D. Zhitomirsky and E. H. Sargent, *Adv. Mater.*, 2012, **24**, 6295–6299.
17 S. M. Thon, A. H. Ip, O. Voznyy, L. Levina, K. W. Kemp, G. H. Carey, S. Masala and E. H. Sargent, *ACS Nano*, 2013, **7**, 7680–7688.
18 J. Zhang, J. Gao, E. M. Miller, J. M. Luther and M. C. Beard, *ACS Nano*, 2013, **8**, 614–622.
19 D. Zhitomirsky, O. Voznyy, S. Hoogland and E. H. Sargent, *ACS Nano*, 2013, **7**, 5282–5290.
20 D. Zhitomirsky, O. Voznyy, L. Levina, S. Hoogland, K. W. Kemp, A. H. Ip, S. M. Thon and E. H. Sargent, *Nat. Commun.*, 2014, **5**, 3803.
21 I. J. Kramer, D. Zhitomirsky, J. D. Bass, P. M. Rice, T. Topuria, L. Krupp, S. M. Thon, A. H. Ip, R. Debnath, H.-C. Kim and E. H. Sargent, *Adv. Mater.*, 2012, **24**, 2315–2319.

22 J. Jean, S. Chang, P. R. Brown, J. J. Cheng, P. H. Rekemeyer, M. G. Bawendi, S. Gradečak and V. Bulović, *Adv. Mater.*, 2013, **25**, 2790–2796.
23 H. Wang, T. Kubo, J. Nakazaki, T. Kinoshita and H. Segawa, *J. Phys. Chem. Lett.*, 2013, **4**, 2455–2460.
24 L. Etgar, W. Zhang, S. Gabriel, S. G. Hickey, M. K. Nazeeruddin, A. Eychmüller, B. Liu and M. Grätzel, *Adv. Mater.*, 2012, **24**, 2202–2206.
25 B. Ehrler, K. P. Musselman, M. L. Böhm, F. S. F. Morgenstern, Y. Vaynzof, B. J. Walker, J. L. MacManus-Driscoll and N. C. Greenham, *ACS Nano*, 2013, **7**, 4210–4220.
26 R. L. Z. Hoye, B. Ehrler, M. L. Böhm, D. Muñoz-Rojas, R. M. Altamimi, A. Y. Alyamani, Y. Vaynzof, A. Sadhanala, G. Ercolano, N. C. Greenham, R. H. Friend, J. L. MacManus-Driscoll and K. P. Musselman, *Adv. Energy Mater.*, 2014, **4**, 1301544.
27 I. Mora-Seró, S. Giménez, F. Fabregat-Santiago, R. Gómez, Q. Shen, T. Toyoda and J. Bisquert, *Acc. Chem. Res.*, 2009, **42**, 1848–1857.
28 B. A. Gregg, F. Pichot, S. Ferrere and C. L. Fields, *J. Phys. Chem. B*, 2001, **105**, 1422–1429.
29 H. Wang, E. D. Gomez, Z. Guan, C. Jaye, M. F. Toney, D. A. Fischer, A. Kahn and Y.-L. Loo, *J. Phys. Chem. C*, 2013, **117**, 20474–20484.
30 J. Gao, C. L. Perkins, J. M. Luther, M. C. Hanna, H.-Y. Chen, O. E. Semonin, A. J. Nozik, R. J. Ellingson and M. C. Beard, *Nano Lett.*, 2011, **11**, 3263–3266.
31 K. W. Kemp, A. J. Labelle, S. M. Thon, A. H. Ip, I. J. Kramer, S. Hoogland and E. H. Sargent, *Adv. Energy Mater.*, 2013, **3**, 917–922.
32 J. Tian, Q. Zhang, E. Uchaker, R. Gao, X. Qu, S. Zhang and G. Cao, *Energy Environ. Sci.*, 2013, **6**, 3542–3547.
33 Z. Tachan, I. Hod, M. Shalom, L. Grinis and A. Zaban, *Phys. Chem. Chem. Phys.*, 2013, **15**, 3841–3845.
34 U. Ozgur, Y. I. Alivov, C. Liu, A. Teke, M. A. Reshchikov, S. Dogan, V. Avrutin, S. J. Cho and H. Morkoc, *J. Appl. Phys.*, 2005, **98**, 041301.
35 R. L. Z. Hoye, K. P. Musselman and J. L. MacManus-Driscoll, *APL Mater.*, 2013, **1**, 060701.
36 S. Yodyingyong, X. Zhou, Q. Zhang, D. Triampo, J. Xi, K. Park, B. Limketkai and G. Cao, *J. Phys. Chem. C*, 2010, **114**, 21851–21855.
37 J. Chang and E. R. Waclawik, *J. Nanopart. Res.*, 2012, **14**, 1012.
38 I. Mora-Sero, L. Bertoluzzi, V. Gonzalez-Pedro, S. Gimenez, F. Fabregat-Santiago, K. W. Kemp, E. H. Sargent and J. Bisquert, *Nat. Commun.*, 2013, **4**, 3272.
39 H. Tang, K. Prasad, R. Sanjinès, P. E. Schmid and F. Lévy, *J. Appl. Phys.*, 1994, **75**, 2042–2047.
40 A. Zaban, M. Greenshtein and J. Bisquert, *ChemPhysChem*, 2003, **4**, 859–864.
41 W. B. Berry and P. Longrigg, *Sol. Cells*, 1988, **24**, 321–328.
42 I. Mora-Sero, G. Garcia-Belmonte, P. P. Boix, M. A. Vazquez and J. Bisquert, *Energy Environ. Sci.*, 2009, **2**, 678–686.
43 F. Fabregat-Santiago, G. Garcia-Belmonte, I. Mora-Sero and J. Bisquert, *Phys. Chem. Chem. Phys.*, 2011, **13**, 9083–9118.
44 V. Gonzalez-Pedro, E. J. Juarez-Perez, W.-S. Arsyad, E. M. Barea, F. Fabregat-Santiago, I. Mora-Sero and J. Bisquert, *Nano Lett.*, 2014, **14**, 888–893.